# Hydrogen-induced metallization on the ZnO(0001) surface

W. S. Silva,[1] C. Stiehler,[2,*] E. A. Soares,[3] E. M. Bittar,[4] J. C. Cezar,[1] H. Kuhlenbeck,[2] H.-J. Freund,[2]
E. Cisternas,[5] and F. Stavale[4]

[1]*Brazilian Synchrotron Light Laboratory (LNLS), National Center for Research in Energy and Materials (CNPEM), Campinas, Brazil*
[2]*Fritz-Haber-Institut der Max-Planck-Gesellschaft, Faradayweg 4-6, D-14195 Berlin, Germany*
[3]*Departmento de Física, ICEx, Universidade Federal de Minas Gerais, CP702 Belo Horizonte, MG, Brazil*
[4]*Centro Brasileiro de Pesquisas Físicas, 22290-180 Rio de Janeiro, RJ, Brazil*
[5]*Departamento de Ciencias Físicas, Universidad de La Frontera, Casilla 54-D, Temuco, Chile*

The formation of hydrogen overlayers on the Zn-terminated ZnO(0001) surface has been reexamined by angle-resolved photoemission spectroscopy (ARPES). While low-energy electron diffraction patterns display the same (1 × 1) symmetry for different surface preparations, the electronic structure feature close to the Fermi level shows the formation of electron pockets, compatible with hydrogen-induced metallic states. Using ARPES and density functional theory (DFT) calculations, we show that hydrogen adspecies can also lead to metallization of this zinc-oxide surface in a similar manner as observed previously on ZnO(10$\bar{1}$0) and O-terminated ZnO(000$\bar{1}$). Importantly, our DFT calculations indicate that these electron pockets are formed by $sp$ hybridized states and therefore the angular distribution of the emitted photoelectron is significantly suppressed at the normal emission.

## I. INTRODUCTION

Zinc oxide (ZnO) is the key material in a large number of applications including solar cells, lasers, gas sensors, and photocatalysts [1–4]. From the technological point of view, most of these applications depend on the manufacture of ZnO nanostructures with large surface-to-bulk ratio with an essential control over the surface growth direction and termination [5,6]. Yet, several properties related to the ZnO surface electronic structure, in particular those connected to its polar surfaces, remain unclear.

Zinc oxide crystallizes into a wurtzite structure, characterized by alternate Zn and O atomic planes, arranged in double layers separated along the $c$ axis by a single Zn-O bond. The cleavage perpendicular to the $c$ axis results in two polar surfaces: Zn-terminated ZnO(0001) and O-terminated ZnO(000$\bar{1}$) [7–9]. For charge neutralization, ZnO polar surfaces undergo various crystallographic and electronic changes depending on the surface termination [8]. In general, the surface displays charge rearrangement, required to cancel the macroscopic electrostatic dipole through the removal of surface atoms and/or adsorption of positively (or negatively) charged adspecies [7].

A number of experimental observations and theoretical calculations suggest that polarity compensation differs on each surface, as well as oxygen and hydrogen coverage [9–16]. The most widely accepted model to achieve charge neutrality in UHV-sputter-cleaned ZnO(0001) involves either the rearrangement of the topmost layer with removal of 1/4

Zn adatoms and the formation of *triangular reconstructions* or formation of residual H or OH overlayers [10,11].

Particularly intriguing is the nonreconstructed hydrogen-(1 × 1) surface first reported by Wöll and co-workers [17]. The authors report the formation of a 2H-(1 × 1) surface using He scattering and low-energy electron diffraction experiments, whereas hydrogen atoms are bound to the topmost Zn adatoms and apparently to subsurface O atoms. Later, Valtiner *et al.*, using density functional theory (DFT) calculations, supported the formation of a metastable 2H-(1 × 1) adlayer and argued that it satisfies the electron counting rule (ECR), a fully compensated semiconducting surface [18]. Yet, despite several recent angle-resolved photoemission spectroscopy (ARPES) experimental investigations on the polar Zn-terminated surface, neither additional observations of this H-(1 × 1) overlayer nor its consequences for the surface electronic structure have been reported in the literature [9,15,19].

In the present study, we used ARPES, low-energy electron diffraction (LEED), x-ray photoelectron spectroscopy (XPS), and density functional theory (DFT) calculations to reexamine the electronic structure of the hydrogen-stabilized Zn-terminated (0001) surface. We observed the formation of electron pockets close to the Fermi level, compatible with the formation of an electron accumulation layer related to a hydrogenated surface. These findings are discussed in terms of the underlying mechanism for hydrogenation and reveal the role of hydrogen in stabilizing the nonreconstructed polar Zn surface.

## II. EXPERIMENTAL AND COMPUTATIONAL METHODS

The experiments were carried out in an ultrahigh vacuum (UHV) multichamber facility at the PGM beam line at the Brazilian Synchrotron Light Laboratory (LNLS). The UHV

---

*Present address: Siemens AG, Rohrdamm 88, 14195 Berlin, Germany.

155416-1

system is equipped with standard thin-film preparation facilities and scanning tunneling microscopy (STM), x-ray and ultraviolet photoelectron spectroscopy (XPS/UPS), and LEED. The base pressure was maintained at $\sim 5 \times 10^{-10}$ mbar and lower than $5 \times 10^{-9}$ mbar during sample transfers. ARPES spectra were measured at 300 K using a SPECS PHOIBOS 150 electron analyzer and photon energy of 103.5 eV using light incident angle of 54° and $p$ polarized with the detector axis normal to the sample surface. The pass energy used and the combined beam line and analyzer resolution, including thermal broadening, were 15 eV and 100 meV, respectively, with 0.2° angular resolution. At this photon energy, a significant part of the probed states are surface states with two-dimensional $k$ vectors in the two-dimensional surface Brillouin zone ($\bar{\Gamma}$). The XPS spectra were obtained using a monochromatic Al-K$\alpha$ source with binding energy (BE) calibrated with respect to the Au $4f^{7/2}$ peak set at 84.0 eV. The XPS spectra were recorded at normal takeoff angle and the O $1s$ peak component's analysis was performed using Gaussian-Lorentzian line shapes after Shirley background subtraction. The line shapes and full width at half maximum have been propagated for all spectra. ZnO(0001) single crystals were obtained from Mateck GmbH and presented no apparent charging effects after several sputtering and annealing cycles. Prior to photoemission measurements, all samples were cleaned by 0.1 M hydrochloric acid (HCl) chemical etching cycles followed by flash annealing at 850 K in UHV. LEED measurements were performed in the preparation chamber before the collection of the photoemission spectra. Since the samples were grounded to the spectrometer, the zero of the BE scale can be directly referenced as the Fermi level of the sample and the valence-band (VB) position was determined from the low BE edge of the VB spectra using the approach proposed by Chambers *et al.* [20]. Topographic AFM images were obtained in an interconnected UHV chamber equipped with a STM/AFM Aarhus-150 operated at room temperature using a KolibriSensor (quartz sensor). The sensor used in the experiment had a resonance at $\sim 0.991$ MHz with the quality factor of 16 000–20 000. The oscillation amplitude employed was less than 400 pm.

The band structure calculations were performed under the DFT+$U$ method in slab geometry using the QUANTUM ESPRESSO package [21,22]. Ultrasoft Becke-Lee-Yang-Parr pseudopotentials were used to describe the exchange-correlation potential. The first Brillouin zone was sampled using a $24 \times 24 \times 1$ Monkhorst-Pack mesh while an energy cutoff of 405 eV was used for plane-wave expansion; both preceding DFT parameters were chosen to ensure an accuracy of 1 meV/cell in the convergence. In our calculations, we obtained lattice parameters $a = 3.2488$ Å and $c/a = 1.6020$, which are in good agreement with experimental [23] and previous [10,24] DFT results. Furthermore, we obtained an energy band gap of 3.4 eV and a band structure in accordance with previous experimental and theoretical results [23]. For the study of H adsorption on the ZnO(0001) surface, we chose a slab model with a $2 \times 2$ surface unit cell consisting of six double layers of ZnO separated by vacuum of about 22 Å. The top three double layers of ZnO as well as the adatoms were allowed to relax until the atomic forces were smaller than 0.027 eV/Å. To mimic the bulk substrate, atoms at the bottom

layers were fixed at their bulk positions. Oxygen atoms at the bottom of the slab were passivated by pseudo-H atoms with valence $(1/2)e^-$, which avoids spurious charge transfer from the back surface to the top surface of the slab.

## III. RESULTS AND DISCUSSION

The ZnO surfaces were prepared by several hydrochloric acid etching cycles and subsequent UHV annealing up to 850 K with base pressures better than $2 \times 10^{-9}$ mbar. The surface composition is shown in Fig. 1(a). Sample cleanliness was achieved after the annealing step in UHV since the C $1s$ peak at 286 eV faded [Fig. 1(a)]. After this procedure, we obtained sharp $(1 \times 1)$ LEED patterns displayed in Fig. 1(b) and relatively flat surfaces as verified by topographic atomic force microscopy images obtained *in situ* and depicted in Fig. 1(c). Residual hydrogen seems to persist after the annealing step as indicated by the high-energy peak component in Fig. 1(d) [8]. Additional cycles of argon sputtering and annealing in UHV apparently remove most of the hydrogen adspecies as seen from the component suppression indicated in Fig. 1(c). However, as we proceed with sputtering and annealing cycles, the surface quality slightly decreases, with a broadening of LEED spots (not shown). The intensity of the O $1s$ peak depicted in Fig. 1(d) is related to oxygen species bounded to Zn and hydroxyl groups bounded either to Zn topmost atoms and subsurface O atoms. Therefore, the peak components ratio can be used to estimate the OH coverage based on models described in the literature [25–27]. In our experimental setup, the electron inelastic mean free path ($\lambda$) is $\sim 19$ Å at photoelectron kinetic energy of 956 eV [28]. Assuming that only the outermost layers are hydroxylated, the OH coverage obtained varies from 0.5 (for $1\lambda$) to 2
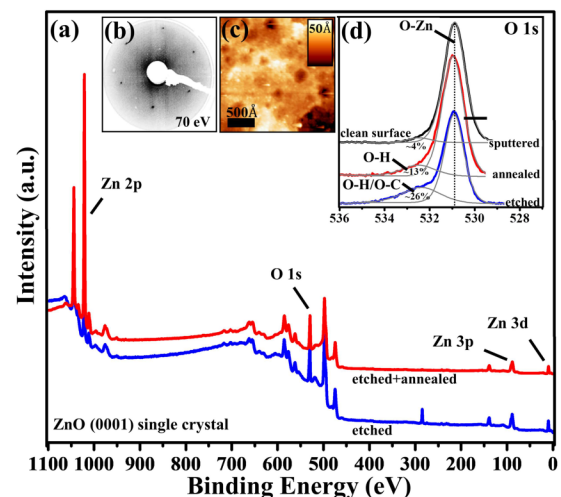


FIG. 1. (a) XPS survey spectra of a ZnO(0001) single-crystal surface after hydrochloric acid etching followed by annealing in UHV at 850 K. The relevant photoemission peaks are indicated. (b) Typical $(1 \times 1)$ LEED pattern and (c) topographic atomic force microscopy image obtained for the clean surface after the etching and annealing procedure. (d) O $1s$ core-level spectra for different sample preparations indicating the presence of hydrogen on the surface. The spectra are offset for clarity.
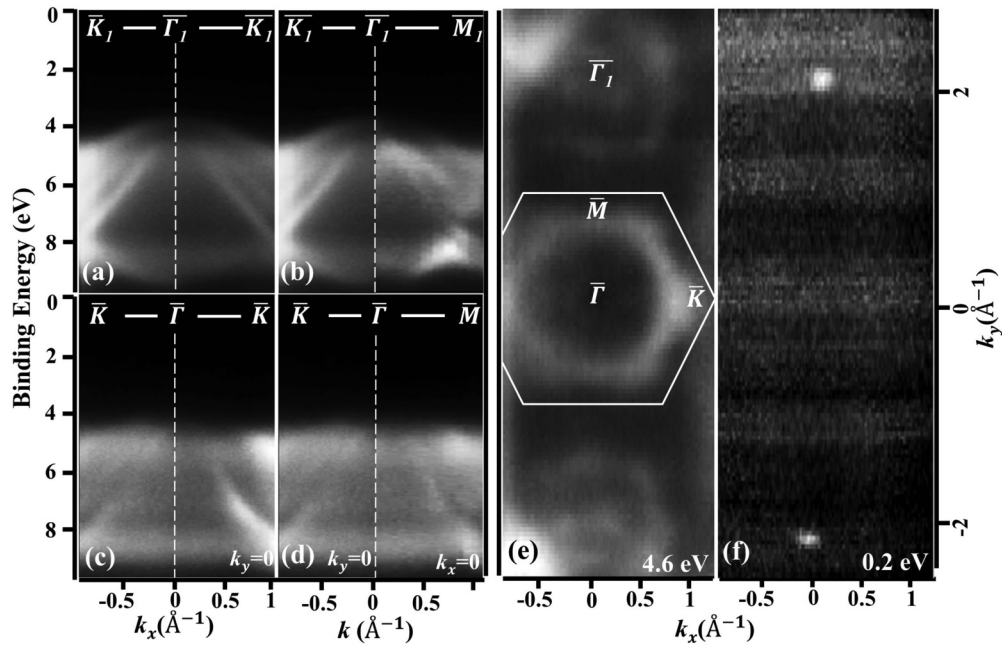
FIG. 2. (a)–(d) ARPES intensity plots for $k_x$ and $k_y$ scans in the $\bar{\Gamma}$-$\bar{M}$-$\bar{K}$ planes at the first ($\bar{\Gamma}$) and second ($\bar{\Gamma}_1$) surface Brillouin zones of ZnO(0001). The scan directions along $\bar{\Gamma}\bar{K}$ and $\bar{\Gamma}\bar{M}$ are shown in (a) and (c); (b) and (d), respectively. (e),(f) Constant-energy contour plots for photoemission intensity in the $\bar{\Gamma}$-$\bar{M}$-$\bar{K}$ planes for 4.6 and 0.2 eV, respectively. (e) indicates the corresponding Brillouin zone, as well as the high-symmetry points and directions calculated using the crystal bulk lattice values.

monolayers, when taking into account the exponential decay of the signal contribution (for $3\lambda$). For this reason, we argue that the OH coverage possibly extensively hydroxylates the surface, although the employed estimative models are based on a flat rather than multilayered surface. The surface roughness is partially promoted by the chemical etching procedure, in agreement with the AFM image depicted in Fig. 1(c). In what follows, we focus our attention on the nonsputtered surface, the one solely chemically etched and annealed in UHV up to 850 K [29].

Figures 2(a)–2(d) display the ARPES data in the $k_x$ − $k_y$ space at the first ($\bar{\Gamma}$) and second ($\bar{\Gamma}_1$) surface Brillouin zones for the ZnO surface. The VB maximum is located about $3.3 \pm 0.1$ eV, determined by extrapolating the leading edge of the emission peak. The dispersive bands related to the O2$p$-Zn4$s$ mixed states (from 3.3 to 10 eV) are clearly observed and suggest that the surface is well ordered after the etching and annealing procedures. These dispersive band features are also consistent with the bulk features previously reported for the ZnO(0001) surface [30,31]. In Figs. 2(e) and 2(f), the dispersive features of the bands in the $\bar{\Gamma}$-$\bar{M}$-$\bar{K}$ plane are shown at the constant-energy intensity plots for 4.6 and 0.2 eV, respectively. The $\bar{\Gamma}$-$\bar{M}$-$\bar{K}$ plane, including the $\bar{\Gamma}$ point and the corresponding high-symmetry directions, are indicated in Fig. 2(e), where the overall hexagonal symmetry of the bands is clearly visible. Interestingly, different structures appear around the $\bar{\Gamma}$ and $\bar{\Gamma}_1$ points depicted in Fig. 2(e). These features demonstrate that the effects related to the angular variation of the electron emission intensity affect band visualization because much weaker photoemission is observed at the top of the valence-band normal $\bar{\Gamma}$ point than at the off-normal $\bar{\Gamma}_1$ points as one compares the constant-energy intensity plots around $\bar{\Gamma}$ and $\bar{\Gamma}_1$ in Fig. 2(e). Noteworthy is that

although not clearly visible in the ARPES maps [Figs. 2(a) and 2(b)] because of the image contrast, one can also note, in Fig. 2(f), features related to dispersive bands appearing just below $E_F$, at 0.2 eV for the off-normal emission (these features appear about 100 times less intense than the top of the valence band located at 3.3 eV). These dispersive bands appear for the off-normal emission with the surface parallel component expanding in a narrow $k_\parallel$ range of 0.2 Å$^{-1}$. This is an important finding since previous studies on the Zn-terminated ZnO(0001) have not reported on states within the band gap originating from bulk or related to adsorption of molecular species [15,19].

The detailed features related to this band are displayed in Fig. 3. The ARPES intensity plots here are obtained by applying the curvature method to the raw ARPES data allowing us to investigate the spectral features close to the $E_F$ [32]. Figures 3(a) and 3(b) show the band dispersion for the $\bar{\Gamma}_1$ $\bar{K}$ and $\bar{\Gamma}_1$ $\bar{M}$ directions, respectively, and Fig. 3(c) depicts the corresponding constant-energy intensity plots at 40 meV. The band exhibits a parabolic behavior with isotropic features running along the ZnO surface high-symmetry directions. The superimposed dashed parabolas can reproduce the bands quite well, with bottom energy at ∼0.2 eV. This band nearly disperses, crossing the $E_F$ with $k_x$ at ±0.1 Å$^{-1}$ for the $\bar{\Gamma}_1$ $\bar{K}$ direction, but it is centered close to the $\bar{\Gamma}_1$ symmetry point at $k_y = 2.26$ Å$^{-1}$ for the $\bar{\Gamma}_1$ $\bar{M}$ direction.

Considering that the ARPES intensity plots for the sputtered and annealed surface do not carry any feature inside the band gap (not shown), one may expect these electronic states for the solely etched and moderate annealed surface to be related to residual adsorbed species on the surface. This assumption is supported by the effective electron mass ($m^*$)
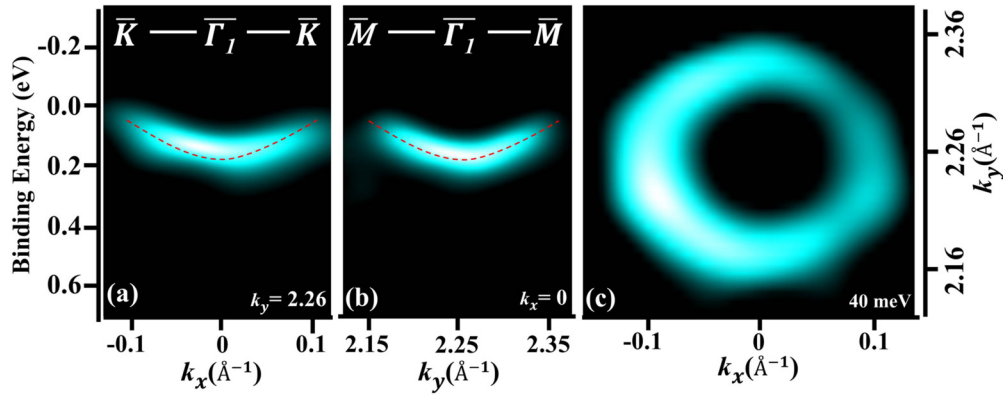
FIG. 3. (a),(b) ARPES intensity plots of the dispersive features close to the $E_F$ of the ZnO(0001) surface along two high-symmetry axes, $\bar{\Gamma}_1\bar{K}$ and $\bar{\Gamma}_1\bar{M}$, respectively. The dashed lines through the plots indicate fitted parabolas assuming parabolic energy-dispersion bands. (c) Fermi surface map centered at $k_x = 0$ and $k_y 2.26 \,\text{Å}^{-1}$ at 40 meV binding energy.

obtained from the parabolic fitting displayed in Fig. 3 using $0.13m_e$. This band displays quite similar features to those observed for hydrogen-induced bands on the ZnO($10\bar{1}0$) and ($000\bar{1}$) surfaces reported by Ozawa *et al.* and Piper *et al.*, although their results on the Zn-terminated surface have not addressed this polarity compensation mechanism [15,19,33]. Here, by assuming the Fermi surface with the radius $k_F = 0.09 \,\text{Å}^{-1}$, the calculated charge density obtained is as large as $3 \times 10^{13} \,\text{cm}^{-2}$, which is readily comparable to the values found for the hydrogen-induced bands on ($10\bar{1}0$) and ($000\bar{1}$) surfaces. Note that although the bands are quite similar in energy position and $\Delta k$ dispersion range, their features are not emerging at normal emission, but actually centered at higher-order $\bar{\Gamma}_1$ symmetry points.

These findings contrast to previous ARPES studies by Ozawa *et al.* and Piper *et al.* and indicate that Zn termination can also be charge compensated by an ordered hydrogen overlayer [15]. In fact, hydrogen-compensated ZnO (0001) has been previously reported by Becker *et al.* using He-scattering experiments, as well as by DFT calculations by Valtiner *et al.* [17,18]. Valtiner *et al.* have explored metastable phases that can be stabilized by hydrogen adsorption on the surface topmost layer. Their proposal is that Zn atoms and step edges can be saturated by hydrogen, including the protonation of O subsurface atoms. This structure shares the hexagonal symmetry of the surface lattice and contains hydrogen atoms bound to both Zn adatoms and subsurface oxygen. Hydrogen bonding to surface and subsurface atoms is consistent with several experimental and theoretical reports on ZnO [16,34–36]. However, under severe hydrogenation conditions, hydrogen is expected to interact with subsurface oxygen atoms by breaking their back bond with the Zn topmost layer, which ultimately leads to the formation of hydroxyl groups and disruption of the surface order by forming either a mixed hydroxide or simply roughing the surface. Nevertheless, under our experimental conditions, the adsorbed hydrogen may maintain a relatively ordered surface structure and, therefore, the induced bands can be visualized in our ARPES intensity plots.

To further clarify the metallic nature of the surface, we have considered that the intensity of the OH contribution in Fig. 1(d), although relatively small, serves as an indication of hydrogen adsorbed on the surface. First of all, we have performed calculations taking into account a $(2 \times 1)$ OH overlayer as previously proposed by Valtiner *et al.* [18]. We noted, however, that as the OH groups adsorb on the surface, the polarity is removed and the oxide band gap is restored to its bulk value, as well as no Fermi energy crossing is observed. For this reason, the surface electronic structure was reexamined for clean, 0.25, 0.5, and 1.0 ML of hydrogen adsorbed on top sites and a fcc hollow site on the $(1 \times 1)$ ZnO surface using the unit cells depicted in Fig. 4. The DFT calculations were found to be consistent with the experimental results when 1 ML of hydrogen is adsorbed on the ZnO surface. In Fig. 5(a) is shown the $k$-resolved band structure of the total density of states (the sum of the topmost surface atoms and bulk atoms), followed by the contribution from each surface atom orbital to the electronic structure of the clean surface. The position of the calculated valence band was aligned to the top of the experimentally observed band structure. Even though there is a general agreement with the experimental data shown in Fig. 2, the conduction band slightly crosses the Fermi level and the calculated band gap is narrower than the experimental one. Noteworthy is that although the clean surface at this condition is expected to be only metastable, since polarity is not yet removed, it serves to indicate trends of the consequences on the electronic structure of the hydrogen adsorption at specific sites. Nevertheless, we note that the experimental valence-band features are quite well described by the calculations whereas the upper part is related to the O $2p$ orbitals and the lower part to the Zn $3d$ orbitals, which are also consistent with earlier reports in the literature [36–39].

Next, we analyze the hydrogen-induced features shown in the $k$-resolved band structure depicted in Fig. 5(b) for the surface saturated with hydrogen adsorbed on both the zinc topmost atoms and oxygen subsurface atoms (according to the Valtiner *et al.* proposal), Fig. 5(c) for the surface saturated with hydrogen adsorbed on the subsurface oxygen layer (according to the Nishidate *et al.* proposal), Fig. 5(d) for the surface saturated with hydrogen adsorbed on the zinc topmost atom (according to the Becker *et al.* proposal), and Fig. 5(e) for hydrogen atoms adsorbed on every fcc hollow surface site (according to the Nishidate *et al.* proposal). In Figs. 5(b) and 5(c), one can note major discrepancies with
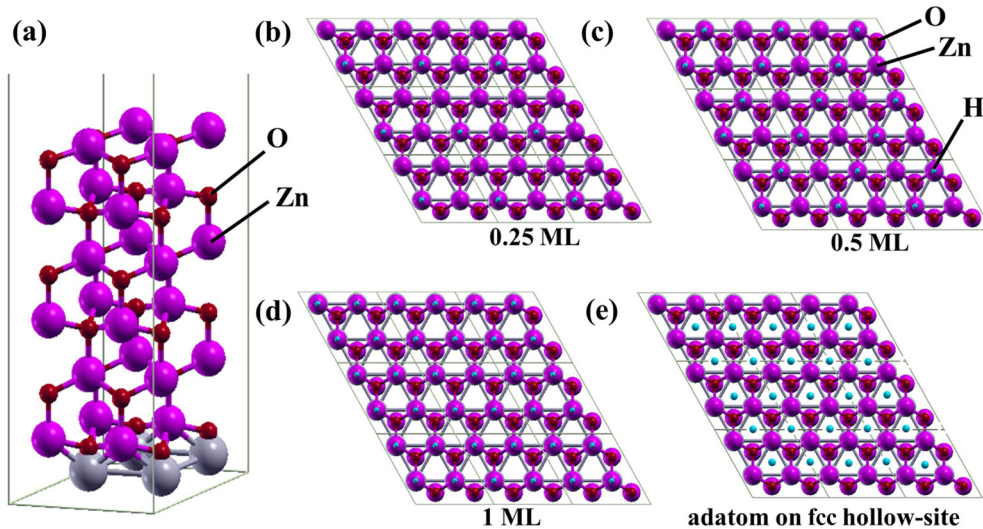
FIG. 4. (a) Unit cell employed in the DFT calculations with O atoms in red, Zn atoms in pink, and pseudo-H atoms in gray. Adsorbed H atoms (in blue) for (b) 0.25, (c) 0.5, and (d) 1.0 ML on top sites and (e) for hydrogen adsorbed on the fcc hollow site.

the experimental data seen in Fig. 2. The total density of states is characterized by several bands crossing the Fermi energy as well as new dispersive features [for Fig. 5(b)] around -8 eV which has not been observed in the experimental data. Moreover, the contribution from the surface oxygen $2p_x$ orbitals to the top of the valence band appears shifted toward larger binding energies. Indeed, band-bending effects are expected to occur on the hydrogenated Zn-terminated surface, however with the top of the valence band shifting toward smaller band energies, causing an overall band gap narrowing. In our experiments, however, additional evidence for the band-gap narrowing and downward shift is not observed since the valence-band maximum appears relatively unchanged comparing the etched and annealed surface to the sputtered and annealed one. In fact, in a recent study, Heinhold *et al.* have shown a valence-band shift of only 20 meV for a Zn-terminated surface prepared by annealing in vacuum as compared to $10^4$ Langmuir hydrogen exposures, a shift much smaller than our experimental uncertainty range of 100 meV [9]. This behavior highlights some of the significant differences between the O- and Zn-polar surfaces decorated with hydrogen, whereas for the Zn termination, band bending is remarkably less affected as compared to the O-terminated surface.

Further, the calculated band structures that better describe the experimental dispersive features are displayed in Figs. 5(d) and 5(e). The $k$-resolved DOS of the hydrogen adsorbed on the Zn topmost atoms and hollow sites show valence bands features between 4 and 7 eV, as well as, $2p_x$ oxygen orbital contributions slightly downward shifted, and a new dispersive feature within the band gap, although the former is not located at 0.2 eV. In addition, the calculated pocket dispersion is significantly smaller in both cases than the one observed experimentally. We argue that the hydrogen, zinc, and oxygen surface atoms' bond-length deviations may affect the calculated band positions and dispersion [40–42]. Nevertheless, the calculations reveal that the most favorable hydrogen adsorption occurs on the Zn topmost atoms, with

formation energy for Zn-H of −1.96 eV as compared to O-H of −1.12 eV and H on the hollow site of −1.75 eV. Therefore, the theoretical results suggest that metastable mixed hydrogen phases may coexist on the surface and account for the discrepancies between the calculated and experimental observed band. Interestingly, one can ascertain from the $k$-resolved projected DOS depicted in Figs. 5(d) and 5(e) that this localized induced state is particularly related to the $s$ orbital of the adsorbed hydrogen atom; and the $2p$ oxygen orbital likewise contributes significantly to the induced localized state. This contribution from the $2p$ orbitals to the localized state occurs essentially for the first subsurface oxygen atoms as compared to deeper layers on the ZnO surface. Thus, although the electronic structure at the Fermi level receives a major contribution from $4s$ Zn orbitals, the interaction with the $2p$ oxygen orbitals leads to the formation of hybridized $sp$-like orbitals. For this reason, the hydrogen atom adsorbed on the Zn-terminated surface induces the development of antibonding $p$ orbitals on the subsurface oxygen atoms, a behavior also consistent with previous DFT studies performed by Nishidate *et al.* and Sanchez *et al.* [16,36]. In addition, we claim from the intensity of the orbital contributions in Fig. 5(d) that the hybridization of the $1s$ occurs somewhat stronger between the $2p_x$ (and $p_y$) orbitals than the $p_z$, since the $1s$ contribution at the $\Gamma$ point appears weaker than at the borders of the surface Brillouin zone (SBZ) leading to a $k$-dependent hybridization.

The hybridization has major consequences for the ARPES intensity plots since the directional character of the electron pockets could only be revealed if the necessary sample rotation to reproduce the $k_y$ dimension is performed as discussed extensively in a recent review from Moser [43]. This state orbital symmetry is the main reason for the electron pockets observation in the adjacent surface Brillouin zones, $\bar{\Gamma}_1$ [see Fig. 2(f)], instead of at the normal emission $\bar{\Gamma}$ point, although photoemission cross sections are also expected to play a role. One can also observe consequences of the orbital symmetry from the $p$-orbital features at the top of the valence bands
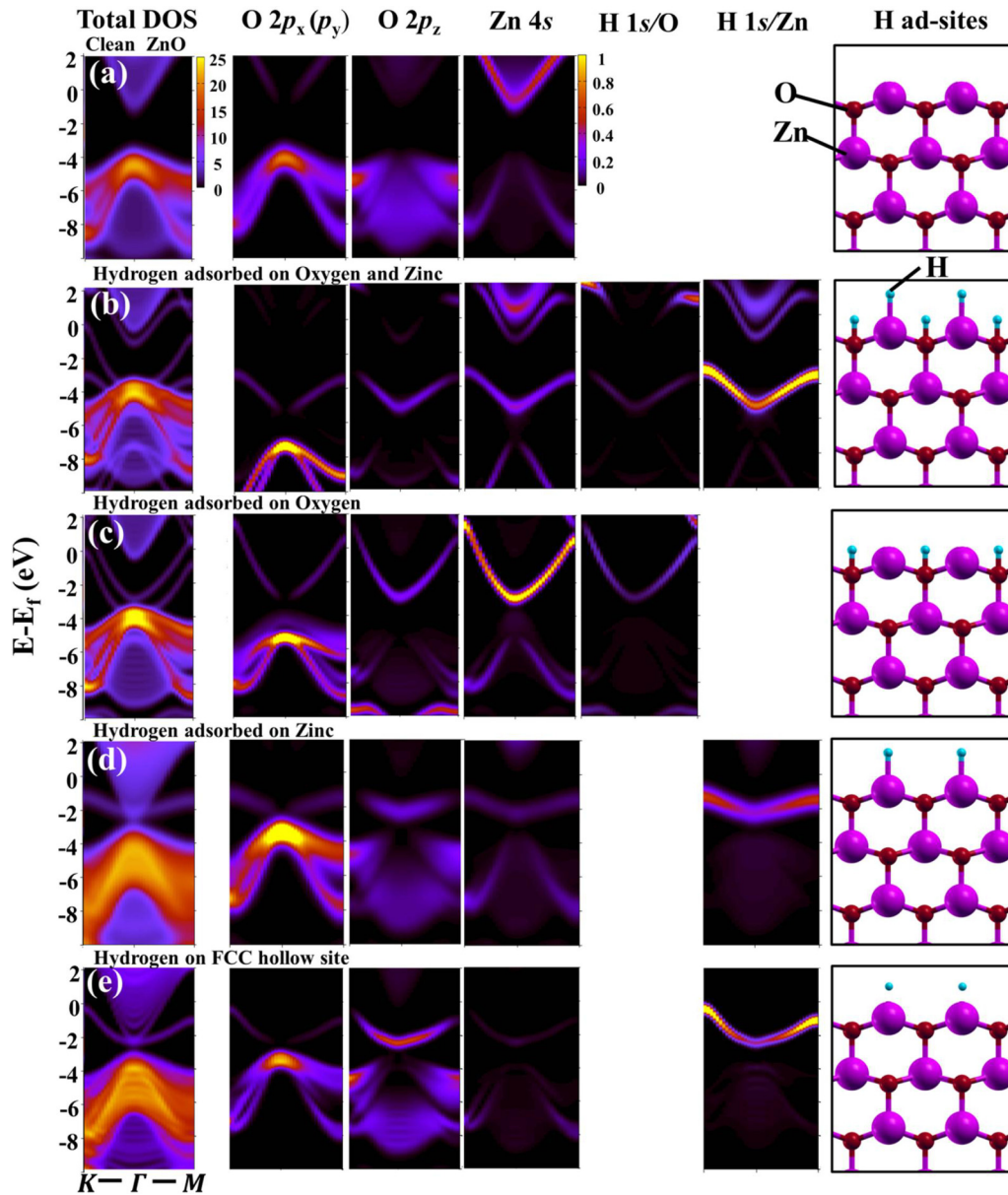
FIG. 5. *k*-resolved band structure calculations for the total density of states and each surface atom orbital contribution along the $\Gamma K$ and $\Gamma M$ directions for (a) clean $(1 \times 1)$ ZnO (0001) surface; (b) hydrogen adsorbed on zinc and oxygen topmost atoms; (c) hydrogen adsorbed on oxygen subsurface atoms; (d) hydrogen adsorbed on zinc topmost atoms; and (e) hydrogen adsorbed on fcc hollow sites. The hydrogen adsorption sites employed in the DFT calculations are shown in the right column with O atoms in red, Zn atoms in pink, and H atoms in blue.

shown in Figs. 2(b) and 2(d), as the valence band appears quite faint at the $\bar{\Gamma}$ point compared to the $\bar{\Gamma}_1$. In our experiments, the top of the valence band features share similar features to those observed previously by Lim *et al.* and Ozawa *et al.* for a clean Zn- and O-terminated ZnO surface [44,45]. The orbital symmetry impact on electron pocket visualization is essential to understand the absence of these electron pockets in previous studies [15]. The reason is that the angular distribution of photoelectrons emitted from $sp$ orbitals using polarized light causes significant suppression of spectral weight at normal emission ($\bar{\Gamma}$). This happens because the light polarization vector suppresses all spectral components in the plane perpendicular to the incoming light polarization [43].

Comparing Zn- and O-terminated surfaces, one can also make symmetry arguments about what to observe in each case. In the first case, we expect that hydrogen adsorbed on Zn lead to $C3v$ symmetry. In this, the twofold-degenerate irreducible representation $E$ to which the oxygen hybridized orbitals $p_x$ and $p_y$ belong is expected to not be very intense in normal emission. In contrast, the hydrogen-decorated O-terminated surface would result in oxygen $p_z$-like orbitals strongly hybridizing with the H $1s$, which is a totally symmetric representation $A_1$, with good intensity at the normal emission. Therefore, in our experiments, because the off-normal emission breaks the symmetry that normally causes an exact cancellation of the scattering of the hydrogen-oxygen

hybridized orbitals, the electron pockets are better visualized at the $\bar{\Gamma}_1$ points.

Finally, in addition to the hybridization process, the photoionization cross sections of H $1s$ and O $2p$ are also expected to play an important role in the pockets observation since the cross sections at the photon energy employed are $\sim$0.01 and 1 Mbarn, respectively [46]. These cross-section values are in close agreement with the intensity ratio observed for the pockets as compared to the top of the valence band (in Fig. 2). As a consequence, the contribution and directional character of the O $2p$ over the symmetric H $1s$ orbitals rule the pocket visualization. For this reason, further ARPES experiments using 20–30 eV photon excitation energies (where H $1s$ and O $2p$ cross sections are $\sim$1 and 5 MBarn, respectively) are needed to absolutely elucidate the mechanism related to the pockets' visualization.

## IV. CONCLUSION

In conclusion, the present results offer direct evidence that hydrogen-induced metallization can also be responsible for surface stabilization on the Zn-terminated ZnO(0001) surface. Although the most widely established model for the polarity compensation of the Zn-terminated surface is related to surface *triangular reconstructions*, whereas the role of hydrogen adsorption may be dismissed, other accessible, and most probable metastable, hydrogenated surface phases may also lead to surface stabilization. This interpretation is not only in line with our measurements and theoretical calculations but also in agreement with the previous reports of Becker *et al.*, Valtiner *et al.*, and Sanchez *et al.* [17,18,36]. For this reason, we believe that the strong surface-localized character of the metallic band is highly related to Zn-terminated surface reactivity. This effect is of fundamental importance for ZnO-based nanostructures, particularly to those connected to optoelectronic applications, since control over the surface termination is crucial. Note that the delicate balance between several stabilization mechanisms and between surface structure geometries is expected to significantly affect areas of application in wet environments, such as photocatalysis and corrosion.

[1] J. X. Wang, X. W. Sun, Y. Yang, H. Huang, Y. C. Lee, O. K. Tan, and L. Vayssieres, Nanotechnology **17**, 4995 (2006).

[2] S. H. Dalal, D. L. Baptista, K. B. K. Teo, R. G. Lacerda, D. A. Jefferson, and W. I. Milne, Nanotechnology **17**, 4811 (2006).

[3] A. B. Djurišić, X. Chen, Y. Hang Leung, and A. Man Ching Ng, J. Mater. Chem. **22**, 6526 (2012).

[4] X. Liu, M-H. Liu, Y-C. Luo, C-Y. Mou, S. D. Lin, H. Cheng, J-M. Chen, J-Fu Lee, and T.-S. Lin, J. Am. Chem. Soc. **134**, 10251 (2012).

[5] Ü. Özgür, Ya. I. Alivov, C. Liu, A. Teke, M. A. Reshchikov, S. Doğanc, V. Avrutin, S.-J. Cho, and H. Morkoç, J. Appl. Phys. **98**, 041301 (2005).

[6] M. H. Huang, S. Mao, H. Feick, H. Yan, Y. Wu, H. Kind, E. Weber, R. Russo, and P. Yang, Science **292**, 1897 (2001).

[7] C. Noguera, J. Phys.: Condens. Matter **12**, R367 (2000).

[8] C. Wöll, Prog. Surf. Sci. **82**, 55 (2007).

[9] R. Heinhold, G. T. Williams, S. P. Cooil, D. A. Evans, and M. W. Allen, Phys. Rev. B **88**, 235315 (2013).

[10] G. Kresse, O. Dulub, and U. Diebold, Phys. Rev. B **68**, 245409 (2003).

[11] O. Dulub, U. Diebold, and G. Kresse, Phys. Rev. Lett. **90**, 016102 (2003).

[12] J. Lahiri, S. Senanayake, and M. Batzill, Phys. Rev. B **78**, 155414 (2008).

[13] R. Lindsay, C. A. Muryn, E. Michelangeli, and G. Thornton, Surf. Sci. **565**, L283 (2004).

[14] M. Valtiner, M. Todorova, G. Grundmeier, and J. Neugebauer, Phys. Rev. Lett. **103**, 065502 (2009).

[15] L. F. J. Piper, A. R. H. Preston, A. Fedorov, S. W. Cho, A. DeMasi, and K. E. Smith, Phys. Rev. B **81**, 233305 (2010).

[16] K. Nishidate and M. Hasegawa, Phys. Rev. B **86**, 035412 (2012).

[17] Th. Becker, St. Hövel, M. Kunat, Ch. Boas, U. Burghaus, and Ch. Wöll, Surf. Sci. **486**, L502 (2001).

[18] M. Valtiner, M. Todorova, and J. Neugebauer, Phys. Rev. B **82**, 165418 (2010).

[19] K. Ozawa and K. Mase, Phys. Rev. B **83**, 125406 (2011).

[20] S. A. Chambers, T. Droubay, T. C. Kaspar, and M. Gutowski, J. Vac. Sci. Technol. B **22**, 2205 (2004).

[21] M. Cococcioni and S. de Gironcoli, Phys. Rev. B **71**, 035105 (2005).

[22] P. Giannozzi, S. Baroni, N. Bonini *et al.*, J. Phys.: Condens. Matter **21**, 395502 (2009).

[23] W. Göpel, J. Pollmann, I. Ivanov, and B. Reihl, Phys. Rev. B **26**, 3144 (1982).

[24] B. Meyer and D. Marx, Phys. Rev. B **67**, 035403 (2003).

[25] P. Liu, K. Kendelewicz, G. E. Brown, and G. A. Parks, Surf. Sci. **412/413**, 287 (1998).

[26] S. Yamamoto, T. Kendelewicz, J. T. Newberg, G. Ketteler, D. E. Starr, E. R. Mysak, K. J. Andersson, H. Ogasawara, H. Bluhm, M. Salmeron, G. E. Brown, and A. Nilsson, J. Phys. Chem. C **114**, 2256 (2010).

[27] E. Carrasco, M. A. Brown, M. Sterrer, H.-J. Freund, K. Kwapien, M. Sierka, and J. Sauer, J. Phys. Chem. C **114**, 18207 (2010).

[28] The inelastic mean free path was calculated using the QUASES-IMFP-TPP2M software, V 3.0.

[29] We have found the same ARPES features for the clean sputtered and annealed ZnO (0001) surface after $\sim$2000L $H_2$ exposure ($P_{H2} \sim 1 \times 10^{-6}$ mbar at 300–400 K).

[30] M. Kobayashi, G. S. Song, T. Kataoka, Y. Sakamoto, A. Fujimori, T. Ohkochi, Y. Takeda, T. Okane, Y. Saitoh, H. Yamagami, H. Yamahara, H. Saeki, T. Kawai, and H. Tabata, J. Appl. Phys. **105**, 122403 (2009).

[31] R.T. Girard, O. Tjernberg, G. Chiaia, S. Söderholm, U. O. Karlsson, C. Wigren, H. Nylén, and I. Lindau, Surf. Sci. **373**, 409 (1997).

[32] P. Zhang, P. Richard, T. Qian, Y.-M. Xu, X. Dai, and H. Ding, Rev. Sci. Instrum. **82**, 043712 (2011).

[33] K. Ozawa and K. Mase, Phys. Rev. B **81**, 205322 (2010).

[34] J.-C. Deinert, O. T. Hofmann, M. Meyer, P. Rinke, and J. Stähler, Phys. Rev. B **91**, 235313 (2015).

[35] M. Hellstrom, I. Beinik, P. Broqvist, J. V. Lauritsen, and K. Hermansson, Phys. Rev. B **94**, 245433 (2016).

[36] N. Sanchez, S. Gallego, J. Cerdá, and M. C. Muñoz, Phys. Rev. B **81**, 115301 (2010).

[37] C. A. Ataide, R. R. Pela, M. Marques, L. K. Teles, J. Furthmuller, and F. Bechstedt, Phys. Rev. B **95**, 045126 (2017).

[38] H. Meskine and P. A. Mulheran, Phys. Rev. B **84**, 165430 (2011).

[39] J. Wróbel, K. J. Kurzydłowski, K. Hummer, G. Kresse, and J. Piechota, Phys. Rev. B **80**, 155124 (2009).

[40] Q. Yan, P. Rinke, M. Winkelnkemper, A. Qteish, D. Bimberg, M. Scheffler, and C. G. Van de Walle, Semicond. Sci. Technol. **26**, 014037 (2011).

[41] M. Oshikiri, Y. Imanaka, F. Aryasetiawan, and G. Kido, Phys. B: Condens. Matter **298**, 472 (2001).

[42] S. Zh. Karazhanov, P. Ravindran, U. Grossner, A. Kjekshus, H. Fjellvåg, and B. G. Svensson, Solid State Commun. **139**, 391 (2006).

[43] S. Moser, J. Electron Spectrosc. Rel. Phenom. **214**, 29 (2017).

[44] K. Ozawa, Y. Oba, K. Edamoto, M. Higashiguchi, Y. Miura, K. Tanaka, K. Shimada, H. Namatame, and M. Taniguchi, Phys. Rev. B **79**, 075314 (2009).

[45] L. Y. Lim, S. Lany, Y. J. Chang, E. Rotenberg, A. Zunger, and M. F. Toney, Phys. Rev. B **86**, 235113 (2012).

[46] The photoionization cross-sections were obtained at https://vuo.elettra.eu/ based on results published at J. J. Yeh, Atomic Calculation of Photoionization Cross-Sections and Asymmetry Parameters, Gordon and Breach Science Publishers, Langhorne, PE (USA), 1993; J. J. Yeh and I. Lindau, Atomic Data and Nuclear Data Tables, 32, 1-155 (1985).